Tropospheric tidal effects on the middle and upper atmosphere

M. E. Hagan, A. Maute, and R. G. Roble

High Altitude Observatory, National Center for Atmospheric Research, Boulder, CO, USA

Abstract

Numerical experiments that explore the effects of tides of tropospheric origin on the upper and middle atmosphere reveal strong signatures of an eastward propagating zonal wavenumber-3 diurnal tide (DE3), which peaks near 110 km and penetrates into the upper thermosphere. We demonstrate that DE3 dissipation in the upper mesosphere and lower thermosphere (MLT) strongly accelerates the zonal mean wind field, affecting both the altitude and magnitude of the low latitude jets. We also quantify, for the first time, a stationary planetary wave-4 oscillation (sPW4) in the MLT, which is excited by nonlinear interaction between the DE3 and the migrating diurnal tide (DW1). Our results suggest that the sPW4 modulates the DE3 MLT response and may impact the E-region dynamo as well as ionospheric and thermospheric signatures aloft.

Introduction

Recent satellite borne diagnostics of the low latitude upper atmosphere reveal longitude variations in 1356 nm airglow brightness measurements [e.g., *Sagawa et al.*, 2005; *Immel et al.*, 2006; *England et al.*, 2006b], electron density [*Lin et al.,* 2007, *Lühr et al.,* 2007], electric field [*England et al.*, 2006a; *Kil et al.*, 2007], electrojet

[*Maus and Lühr*, 2007], and thermospheric wind data [*Häusler et al.,* 2007; *Lühr et al.,* 2007] with 4-peaked structures. In their report on the results of a numerical experiment with the thermosphere-ionosphere-mesosphere-electrodynamics general circulation model (TIME-GCM), *Hagan et al.,* [2007] demonstrated that the eastward propagating zonal wavenumber-3 diurnal tide (DE3) could propagate from the troposphere into the lower thermosphere, modulate the E-region dynamo process, and thereby introduce a 4-peaked F-region wave structure when observed from Sun-synchronous orbit. This simulation included global-scale wave model (GSWM) forcing after *Hagan and Forbes* [2002, 2003] at the TIME-GCM lower boundary (ca., 30 km) to account for atmospheric tides of tropospheric origin, including a DE3 component which is excited by latent heat release in deep tropical clouds.

In this report, we highlight the results of a complementary set of TIME-GCM calculations to highlight nonmigrating tidal effects on the neutral atmosphere.

TIME-GCM Simulations

The TIME-GCM is a three-dimensional time-dependent model developed at the National Center for Atmospheric Research (NCAR) and designed to simulate the circulation, temperature, electrodynamics, and compositional structure of the upper atmosphere and ionosphere by calculating neutral gas heating, dynamics, photoionization, electrodynamics, and the compositional structure on a global grid from first principles and for a given solar irradiance spectrum which varies with solar activity. The effects of sub-grid-scale gravity waves are parameterized with a modified *Lindzen* [1981] type scheme that is extended to include molecular damping effects in the lower thermosphere. *Roble and Ridley* [1994], *Roble* [1995; 1996] and references therein provide a more complete description of the TIME-GCM.

Wu et al. (2008a) reported the need to increase the resolution of the TIME-GCM in order to properly resolve diurnal tidal fields. As in *Hagan et al.* [2007], we ran the TIME-GCM with 2.5^{o} by 2.5^{o} horizontal resolution and 4 grid points per scale height in the vertical for the results reported herein; twice the resolution that characterized other earlier simulations. Our focus is solar minmum and geomagnetically quiescent September conditions. Thus, we invoked a 10.7-cm solar radio flux (F10.7) value of 75, a hemispheric power value [after *Evans*, 1987] of 8 GW, and a cross-cap potential drop of 30 kV to respectively represent solar radiative and auroral forcing in our September simulations (i.e., day of year 270).

The TIME-GCM inherently accounts for atmospheric tides that are excited by the absorption of ultraviolet and extreme ultraviolet radiation in the middle and upper atmosphere. We accounted for tidal components of tropospheric origin that propagate upward into the model domain by perturbing the TIME-GCM lower boundary (ca., 10 hPa; ~30 km) with the September tidal fields from the GSWM. These GSWM results

[*Hagan and Forbes*, 2002; 2003] include tropospheric tidal responses excited by the absorption of infrared radiation as well as latent heat release associated with condensation in deep convective clouds in the tropics.

Migrating tides excited by the absorption of solar infrared radiation in the troposphere have long been included in TIME-GCM simulations, since their impacts on the atmosphere aloft are well established [e.g., *Hagan*, 1996; *McLandress et al.*, 1996; *Fesen et al.*, 2000]. However, the TIME-GCM March simulations reported by *Hagan et al.* [2007] represent the first time that nonmigrating (i.e., not Sun-synchronous) tides were introduced at the model lower boundary. We devised a set of TIME-GCM simulations reported herein to further explore nonmigrating tidal effects during September equinox. We conducted a so-called realistic simulation by including all tidal components at the lower boundary along with a control simulation that only included the GSWM diurnal and semidiurnal migrating tides. Differences between the realistic and control simulation results allow us to quantify nonmigrating tidal effects in the TIME-GCM.

Results

The zonal mean zonal winds that characterize the realistic TIME-GCM simulation are illustrated in the left panel of Figure 1 as a function of latitude, pressure level (hereafter PL), and altitude. As expected during equinox these

TIME-GCM mesospheric and lower thermospheric winds are fairly symmetric about the equator. The zonal mean zonal winds are predominantly eastward below about 120 km (PL -4), and westward aloft. The exceptions are a westward jet centered over the equator between 65 and 85 km (PLs -12.5 and -9.5) that exceeds 60m/s and peaks near 80 km (PL -10), and a high northern latitude thermospheric circulation that is driven by the ionospheric convection electric field. The westward jet in the upper mesosphere is driven by parameterized gravity wave effects combined with migrating diurnal tidal dissipation (e.g., *Forbes et al*., 1993).

The northern hemispheric middle atmosphere eastward jet speed exceeds 70 m/s near 35^{o}N and 70 km (PL -12), while the counterpart in the southern hemisphere peaks at 50 m/s near 35^{o}S and 70km. The remaining eastward jet maximizes over the equator in the mesopause region near 100 km (PL -7) with speeds that exceed 60 m/s. The morphology and the salient features of these TIME-GCM winds are consistent with zonal mean zonal wind climatologies. But, the magnitudes of the eastward jets in the middle-upper atmosphere are larger than the zonal mean winds inferred from UARS measurements (e.g., *McLandress et al.*, 1996).

Also illustrated in Figure 1 (right panel) are the wind differences between the realistic and control simulations (i.e., all tides minus migrating tide results), which quantify the effects of the nonmigrating components on the zonal mean circulation.

The characterizing feature is an eastward jet that peaks at 90 km (PL -8.5) over the equator and is confined to +/- 30^{o} and 80 to 110 km. These winds are attributable to the dissipating eastward tidal components, which produce changes in the zonal winds in excess of 50 m/s. This zonal wind acceleration affects both the magnitude and the location of the equatorial jets illustrated in the left panel of Figure 1, shifting the peak westward winds to 75 km. This is 5 km lower and 20 m/s weaker than the corresponding jet is in the absence of the eastward nonmigrating tidal driver (not illustrated). This same acceleration also affects the overlying eastward jet. Not only does the 90-km wind reversal occur approximately 10 km lower than the reversal in the control simulation, the jet is 20m/s stronger with a peak value that exceeds 50 m/s near ~100 km over the equator. While the nonmigrating tides significantly affect the strength of this mesopause region eastward jet, Figure 1 also illustrates that these tides have no impact on the eastward jets in the middle latitude mesosphere.

Figure 2 illustrates the TIME-GCM latitude-height structure of the zonal wind tidal amplitudes associated with the dominant diurnal tidal responses in our realistic simulation, namely, the migrating (i.e., westward propagating zonal wavenumber 1; DW1) and the eastward propagating zonal wavenumber 3 diurnal tide (DE3) tides. As anticipated, the DW1 structure below PL -4 (~120 km) is markedly different from the results aloft (Figure 2; left panel). The DW1 that propagates from the troposphere, upper stratosphere, and lower mesosphere into the mesopause region peaks near +/-25^{o} and PL -6.5 (~102 km). This component is partially excited in the TIME-GCM and also arises from the GSWM lower boundary forcing. The upper thermospheric DW1 amplitude is attributable to the absorption of extreme ultraviolet (EUV) solar radiation in situ and is calculated self-consistently in the model domain. This component increases with increasing altitude above PL -4 (~120 km) with the strongest signatures at high-middle latitudes. The contrasting behavior of the upward propagating and evanescent components of the DW1 in our simulation exhibits the expected salient features of the so-called (1,1) and (1,-2) Hough modes, respectively, as described by classical tidal theory (e.g., *Chapman and Lindzen*, 1970).

In contrast, the DE3 is solely excited in the troposphere and is attributable to the GSWM forcing in our realistic simulation; it does not appear in our control simulation results (not illustrated). The DE3 amplitude (Figure 2; right panel) is consistent with an upward propagating tidal component, increasing with increasing altitude. The peak amplitude near PL -5.5 (~107 km) approaches 45 m/s. Although the DE3 dissipates at higher altitudes, it penetrates well into the TIME-GCM upper thermosphere maintaining amplitudes larger than 15 m/s above PL 0 (~210 km) at equatorial and low latitudes. The behavior of the DE3 is consistent with that of a diurnal Kelvin wave with strong temperature (not illustrated) and zonal wind amplitudes that are largely confined to low latitudes and a comparatively weak meridional wind perturbation (not illustrated).

The DW1 and DE3 tides can interact with one another to produce two waves, the eastward propagating wavenumber-2 semidiurnal tide (SE2) and stationary planetary wave 4 (sPW4). Evidence of the excitation of so-called secondary waves resulting from nonlinear interactions between primary waves from data analyses and in modeling investigations was previously reported [e.g., *Teitelbaum and Vial,* 1991; *Hagan and Roble*, 2001; *Pancheva et al*., 2002] Herein, we report on the first evidence of the excitation of a stationary planetary wave (i.e., sPW4) by the interaction between a migrating and nonmigrating tidal component. This is a definitive result because the sPW4 is not excited at the TIME-GCM lower boundary, and it is not present in the control simulation. This result is particularly important to the interpretation of measurements made by slowly precessing satellites that cannot distinguish between the signatures of the DE3 wave and the SE2 and sPW4 secondary waves on a short-term basis.

Figure 3 illustrates the SE2 (left panel) and sPW4 (right panel) zonal wind amplitudes from our realistic simulation. Unlike the sPW4, the tropospheric latent heat tidal source in the GSWM also includes an SE2, so it is introduced at the TIME-GCM lower boundary. Although the SE2 is comparatively weak (i.e., amplitudes < 10 m/s), it is present throughout most of the model domain. The largest mesopause region SE2 signature is the equatorial ~10 m/s peak at about 100 km (PL -7). There are secondary SE2 peaks midlatitude peaks; ~6 m/s at 45^{o}N and ~107 km (PL -5.5), and in excess of 8 m/s at 40^{o}S and ~140 km (PL -3). The much stronger sPW4 is more confined; there is a single 25 m/s peak centered over the equator at ~105 km (PL -6). Amplitudes of 5-10 m/s characterize the low-mid latitude response throughout the upper mesosphere and lower thermosphere (i.e., 85-120 km; PL ranges from -9 to -4) between about 20^{o} and 35^{o} both north and south of the equator. Notably, equatorial sPW4 amplitudes in excess of 5/ms extend well into the thermosphere above PL 0 (~210 km).

The comparative strength of the aforementioned wave components is readily seen in the equatorial profiles of zonal wind amplitudes from the realistic simulation illustrated in Figure 4, which also includes the migrating semidiurnal tide (SW2) results. The DE3 dominates the response in the upper mesosphere and into the lower thermosphere (i.e., 85-120 km; PL between -9 and -4), peaking at about 45 m/s near ~105 km (PL -6), while the in-situ generated DW1 dominates the response aloft, above ~180 km (PL -1). The DW1 and sPW4 zonal wind amplitudes are significant and comparable throughout much of the equatorial upper mesosphere and lower thermosphere, with peak values in excess of 25 m/s at ~105 km (PL -6). Notably, the

DE3 amplitude remains large (~20 m/s) into the upper thermosphere, where it is comparable to the equatorial SW2 zonal wind perturbation. Both the SE2 and sPW4 also penetrate into the highest part of the TIME-GCM domain but with significantly smaller magnitudes of order 5 m/s.

Discussion and Summary

Observational evidence from space-borne instruments demonstrates that the DE3 is a ubiquitous feature of the low latitude upper mesosphere and lower thermosphere, and that it exhibits strong seasonal variability, maximizing during August-September (e.g. *Forbes et al*., 2003; 2008, *Oberheide et al*., 2006, *Wu et al*., 2008). This suggests that the September TIME-GCM results presented herein represent an upper limit of the potential DE3 impact on the middle and upper atmosphere. Notably, our zonal wind acceleration results (Figure 1) exceed a previous estimate for DE3 effects during August by almost a factor of two. *Forbes et al.* [2006] used a quasi-linear time-dependent model after *Miyahara and Wu* (1989) to simulate a DE3 tide with an equatorial peak temperature amplitude of ~25^{o}K. This produced an effective eastward jet in excess of 20 m/s at low latitudes between about 90 and 120 km. The tidal forcing in the *Forbes et al.* [2006] calculation was explicitly calibrated to approximate the DE3 temperature perturbation observed by the TIMED/SABER satellite instrument during 2002, suggesting that the GSWM climatological September forcing that characterizes our realistic simulation may overestimate the 2002 DE3 excitation. Alternatively, tidal dissipation in the upper mesosphere and lower thermosphere may be underestimated in the TIME-GCM. *Wu et al.,* (2008b) reported that the interannual variability in the TIMED/TIDI DE3 zonal wind tide was of order 14-24 m/s at ~105 km during the months of September in 2002 through 2006. Like the aforementioned SABER results, the TIDI observational diagnostics contain inherent uncertainties associated 60-day-averaging analyses. Nevertheless, our TIME-GCM DE3 winds are significantly (i.e., 15-25 m/s) larger. In spite of the amplitude overestimates, the dynamical features that we report herein, including DE3 propagation into the upper atmosphere, DE3 interaction with the DW1 producing sPW4 and an SE2 tide, and DE3 dissipation and acceleration of the zonal mean flow represent fundamental physical processes that are self-consistently represented in the TIME-GCM.

The TIME-GCM perturbations that we report herein also have implications for the interpretation of wave-4 signatures that are routinely observed in near Sun-synchronous satellite observations of the low-latitude thermosphere and ionosphere, examples of which are referenced in our introduction. Specifically, our investigation demonstrates that the DE3 can penetrate into the upper thermosphere and directly modulate the thermosphere-ionosphere coupling processes at F-region altitudes. Thus, the wave-4 signatures observed in the F-region may result from a combination of these direct effects and the indirect effects produced by DE3 modulation of the E-region dynamo process as described by *Hagan et al.* [2007]. Further, the sPW4 may also modulate the E-region dynamo or propagate into the upper atmosphere and produce a wave-4 signature from Sun-synchronous orbit. The SE2 tide is similarly capable, but our TIME-GCM results suggest that the DE3 drivers dominate the wave-4 ionospheric response with increasingly smaller contributions from the sPW4 and SE2. Although both the DW1 and SW2 are important to the dynamics of the thermosphere, neither play a role in explaining this longitudinal variability, since migrating tides are longitudinally invariant when observed from near Sun-synchronous orbit.

The nonmigrating tidal effects reported herein are even more complicated for comparable TIME-GCM calculations during solstice conditions. These are beyond the purview of this report. However, in the aggregate the TIME-GCM and GSWM results point to unresolved questions regarding tropospheric tidal forcing, warranting additional analyses of tropospheric water vapor, clouds, as well as long and short-wave radiative budgets. In addition, we need to conduct detailed model-measurement comparisons to determine how well the TIME-GCM is capturing the longitudinal tidal variability observed in the stratosphere, mesosphere, and lower thermosphere from space, and by ground-based global networks of radars and lidars.

Acknowledgements.
The authors thank Qian Wu and Jeff Forbes for comments on the initial draft of this report. The National Center for Atmospheric Research is supported by the National Science Foundation.

Reference

Chapman, S., and R. S. Lindzen (1970), *Atmospheric Tides*, 201 pp., D. Reidel, Norwell, Mass.

England, S. L., S. Maus, T. J. Immel, and S. B. Mende (2006a), Longitudinal variation of the E-region electric fields caused by atmospheric tides, *Geophys. Res. Lett.*, *33*, L21105, doi:10.1029/2006GL027465.

England, S. L., T. J. Immel, E. Sagawa, S. B. Henderson, M. E. Hagan, S. B. Mende, H. U. Frey, C. M. Swenson, and L. J. Paxton (2006b), Effect of atmospheric tides on the morphology of the quiet time, postsunset equatorial ionospheric anomaly, *J. Geophys. Res.*, *111*, A10S19, doi:10.1029/2006JA011795.

Evans, D. S., Global Statistical Patterns of Auroral Phenomena (1987), *Proceedings of the Symposium on Quantitative Modeling of Magnetospheric - Ionospheric Coupling Processes*, p. 325, Kyoto Japan.

Fesen, C. G., G. Crowley, R. G. Roble, A. D. Richmond, B. G. Fejer (2000), Simulation of the pre-reversal enhancement in the low latitude vertical ion drifts, *Geophys. Res. Lett.*, 27(13), 1851-1854, 10.1029/2000GL000061.

Forbes, J. M., R. G. Roble, and C. G. Fesen (1993), Acceleration, heating, and composition mixing of the thermopshere due to upward propagating tides, *J. Geophys. Res., 98*(A1), 311–322.

Forbes, J. M., X. Zhang, W. Ward, and E. R. Talaat (2002), Nonmigrating diurnal tides in the thermosphere, *J. Geophys. Res.*, 107(D23), 4322, doi:10.1029/2001JD001232, 2002.

Forbes, J. M. , J. M. Russell III, S. Miyahara, X. Zhang, S. E. Palo, M. Mlynczak, C. J. Mertens, and M. E. Hagan (2006), Troposphere-Thermosphere tidal coupling as measured by the SABER instrument on TIMED during July-September 2002, *J. Geophys. Res.*, 111, A10S06, doi:10.1029/2005JA011492.

Hagan, M. E., and J. M. Forbes (2002), Migrating and nonmigrating diurnal tides in the middle and upper atmosphere excited by tropospheric latent heat release, *J. Geophys. Res.*, *107*(D24), 4754, doi:10.1029/2001JD001236.

Hagan, M. E. and R. G. Roble, Modeling diurnal tidal variability with the NCAR TIME-GCM, *J. Geophys. Res.*, *106*, 24,869-24,882, 2001.

Hagan, M. E., and J. M. Forbes (2003), Migrating and nonmigrating semidiurnal tides in the upper atmosphere excited by tropospheric latent heat release, *J. Geophys. Res.*, *108*(A2), 1062, doi:10.1029/2002JA009466.

Hagan, M. E., A. I., Maute, R. G. Roble, A. D. Richmond, T. J. Immel, and S. L. England (2007), Connections between deep tropical clouds and the Earth's ionosphere, *Geophys. Res. Lett., 34*, L20109, doi:10.1029/2007GL030142.

Häusler, K., H. Lühr, S. Rentz, and W. Köhler (2007), A statistical analysis of longitudinal dependences of upper thermospheric zonal winds at dip equator latitudes derived from CHAMP, *J. Atmos. Solar-Terr. Phys.*, doi:10.1016/j.jastp.2007.04.004.

Immel, T. J., E. Sagawa, S. L. England, S. B. Henderson, M. E. Hagan, S. B. Mende, H. U. Frey, C. M. Swenson, and L. J. Paxton (2006), Control of equatorial ionospheric morphology by atmospheric tides, *Geophys. Res. Lett.*, 33, L15108, doi:10.1029/2006GL026161.

Kil H., S.-J. Oh, M. C. Kelley, L. J. Paxton, S. L. England, E. Talaat, K.-W. Min, S.-Y. Su (2007), Longitudinal structure of the vertical E × B drift and ion density seen from ROCSAT-1, *Geophys. Res. Lett.*, 34, L14110, doi:10.1029/2007GL030018.

Lin, C. H., W. Wang, M. E. Hagan, C. C. Hsiao, T. J. Immel, M. L. Hsu, J. Y. Liu, L. J. Paxton, T. W. Fang, and C. H. Liu (2007), Plausible effect of atmospheric tides on the equatorial ionosphere observed by the FORMOSAT-3/COSMIC: Three-dimensional electron density structures, *J. Geophys. Res.*, *34*, L11112, doi:10.1029/2007GL029265.

Lindzen, R. S. (1981), Turbulence and stress owing to gravity wave and tidal breakdown, *J. Geophys. Res.*, *86*, 9707-9714.

Lühr, H., K. Häusler, and C. Stolle (2007), Longitudinal variation of F region electron density and thermospheric zonal wind caused by atmospheric tides, *Geophys. Res. Lett*. 34, L16102, doi:10.1029/2007GL030639.

Lühr, H., M. Rother, K. Häusler, P. Alken and S. Maus (2008), The influence of non-migrating tides on the longitudinal variation of the equatorial electrojet, *J. Geophys. Res.*, in press.

McLandress, C., G. G. Shepherd, B. H. Solheim, M. D. Burrage, P. B. Hays, and W. R. Skinner (1996), Combined mesosphere/thermosphere winds using WINDII and HRDI data from the Upper Atmosphere Research Satellite, J. Geophys. Res., 101(D6), 10,441–10,453.

Miyahara, S. and D.-H. Wu (1989), Effects of solar tides on the zonal mean circulation in the lower thermosphere: solstice condition. *Journal of Atmospheric and Terrestrial Physics* 51 (1989), 635–647.

Oberheide, J., Q. Wu, T. L. Killeen, M. E. Hagan, and R. G. Roble (2006), Diurnal nonmigrating tides from TIMED Doppler Interferometer wind data: Monthly climatologies and seasonal variations, *J. Geophys. Res.*, *111*, A10S03, doi:10.1029/2005JA011491.

Pancheva, D., E. Merzlyakov, N. J. Mitchell, Yu. Portnyagin, A. H. Manson, Ch. Jacobi, C. E. Meek, Y. Luo, R. R. Clark, W. K. Hocking, J. MacDougall, H. G. Muller, D. Kürschner, G. O. L. Jones, R. A. Vincent, I. M. Reid, W. Singer, K. Igarashi, G. I.

Fraser, A. N. Fahrutdinova, A. M. Stepanov, L. M. G. Poole, S. B. Malinga, B. L. Kashcheyev and A. N. Oleynikov (2002), Global-scale tidal variability during the PSMOS campaign of June–August 1999: interaction with planetary waves, doi:10.1016/S1364-6826(02)00199-2.

Roble, R. G. (1995), Energetics of the mesosphere and thermosphere, *The Upper Mesosphere and Lower Thermosphere: A Review of Experiment and Theory*, AGU Monograph 87.

Roble, R. G. (1995), The NCAR Thermosphere-Ionosphere-Mesosphere-Electrodynamics General Circulation Model (TIME-GCM), *Ionosphere Models*, STEP Handbook on Ionospheric Models (ed. R. W. Schunk), Utah State University.

Roble, R. G., and E. C. Ridley (1994), A thermosphere-ionosphere-mesosphere-electrodynamics general circulation model (TIME-GCM): Equinox solar cycle minimum simulations (30-500 km), *Geophys. Res. Lett., 21*, 417-420.

Sagawa, E., T. J. Immel, H. U. Frey, and S. B. Mende (2005), Longitudinal structure of the equatorial anomaly in the nighttime ionosphere observed by IMAGE/FUV, *J. Geophys. Res*., 110, A11302, doi:10.1029/2004JA010848.

Teitelbaum, H., and F. Vial (1991), On the tidal variability induced by non-linear interaction with planetary waves. Journal of Geophysical Research 96, 14169–14178.

Wu, Q., D. A. Ortland, T. L. Killeen, R. G. Roble, M. E. Hagan, H.-L. Liu, S. C. Solomon, J. Xu, W. R. Skinner, and R. J. Niciejewski (2008a), Global distribution and interannual variations of mesospheric and lower thermospheric neutral wind diurnal tide: 1. Migrating tide, J. Geophys. Res., 113, A05308, doi:10.1029/2007JA012542.

Wu Q., D. A. Ortland, T. L. Killeen, R. G. Roble, M. E. Hagan, H.-L. Liu, S. C. Solomon, J. Xu, W. R. Skinner, R. J. Niciejewski (2008b), Global distribution and interannual variations of mesospheric and lower thermospheric neutral wind diurnal tide: 2. Nonmigrating tide, *J. Geophys. Res*., 113, A05309, doi:10.1029/2007JA012543.

Figure Captions

Figure 1. Contours of TIME-GCM zonal mean zonal wind (m/s) versus geographic latitude and pressure level (lnp0/p)/altitude (km) during September solar minimum conditions (left) and the wind differences (right) that are attributable to nonmigrating

tides of tropospheric origin (right). See text for details.

Figure 2. TIME-GCM migrating (left) and eastward propagating zonal wave number 3 (right) diurnal zonal wind amplitudes (m/s) versus latitude and pressure level (lnp0/p) from the September solar minimum simulation.

Figure 3. Same as Figure 2, except for the eastward propagating zonal wave number 2 semidiurnal (left) and the stationary planetary wave 4 (right) zonal wind amplitudes (m/s).

Figure 4. TIME-GCM equatorial zonal wind amplitude (m/s) profiles for the dominant global waves that characterize the September solar minimum results; the migrating diurnal (solid) and semidiurnal (long dash) tides, the eastward propagating zonal wavenumber 3 diurnal tide (medium dash), the eastward propagating zonal wavenumber 2 semidiurnal tide (short dash), and stationary planetary wave 4 (combination long-short dash).

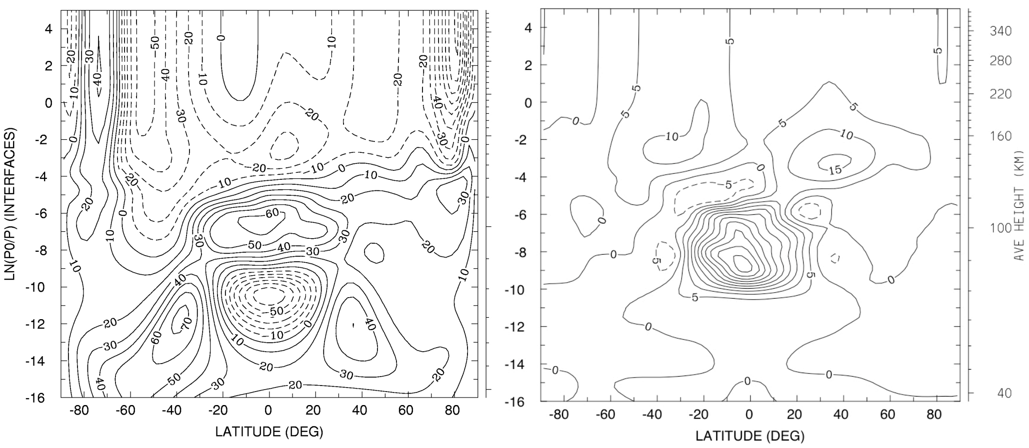

Figure 1. Contours of TIME-GCM zonal mean zonal wind (m/s) versus geographic latitude and pressure level (ln p0/p)/altitude (km) during September solar minimum conditions (left) and the wind differences (right) that are attributable to nonmigrating tides of tropospheric origin (right). See text for details.

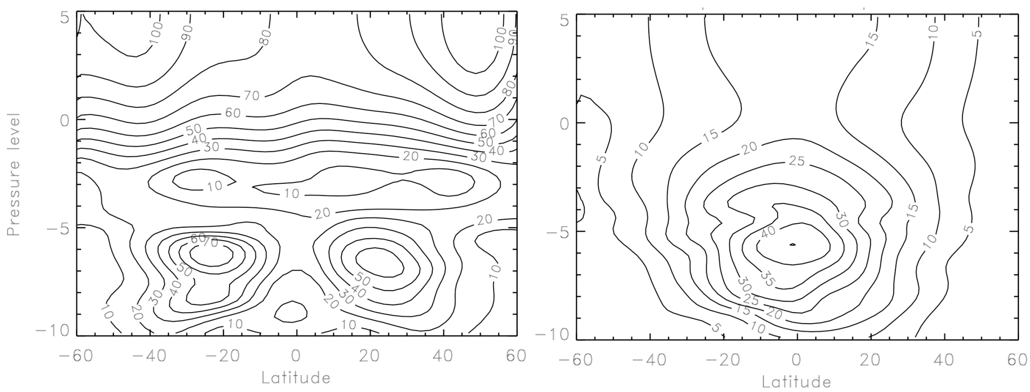

Figure 2. TIME-GCM migrating (left) and eastward propagating zonal wave number 3 (right) diurnal zonal wind amplitudes (m/s) versus latitude and pressure level (lnp0/p) from the September solar minimum simulation.

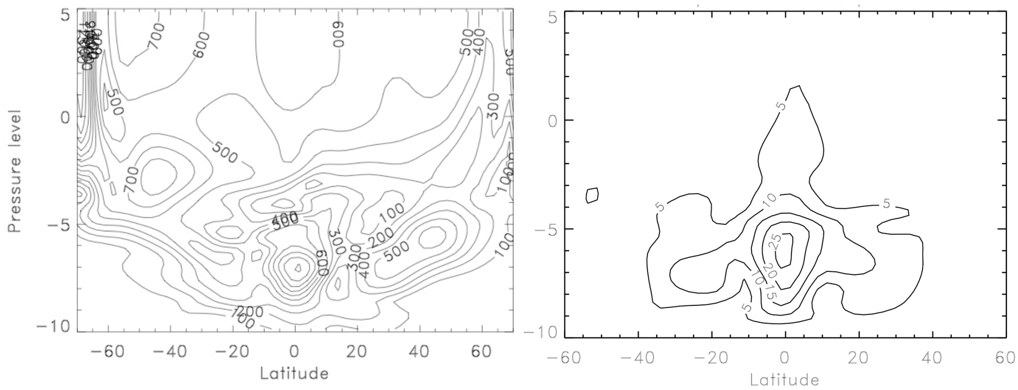

Figure 3. Same as Figure 2, except for the eastward propagating zonal wave number 2 semidiurnal (left; cm/s) and the stationary planetary wave 4 (right; m/s) zonal wind amplitudes

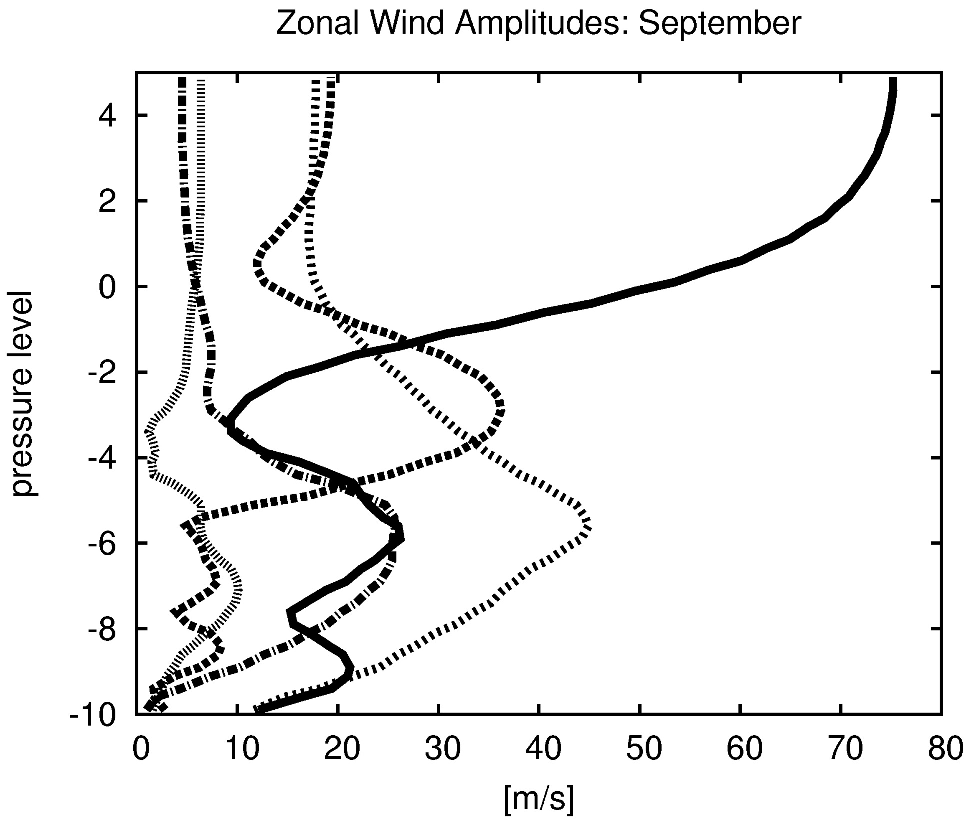

Figure 4. TIME-GCM equatorial zonal wind amplitude (m/s) profiles for the dominant global waves that characterize the September solar minimum results; the migrating diurnal (solid) and semidiurnal (long dash) tides, the eastward propagating zonal wavenumber 3 diurnal tide (medium dash), the eastward propagating zonal wavenumber 2 semidiurnal tide (short dash), and stationary planetary wave 4 (combination long-short dash).